Routing Single Photons from a Trapped Ion Using a Photonic Integrated Circuit

Uday Saha,[1,2,*] James D. Siverns,[1,2,3] John Hannegan,[2,3] Mihika Prabhu,[4] Qudsia Quraishi,[2,5,6]
Dirk Englund,[4] and Edo Waks[1,2,3,6,†]

[1] *Department of Electrical and Computer Engineering, University of Maryland College Park, Maryland 20742, USA*
[2] *Institute for Research in Electronics and Applied Physics (IREAP), University of Maryland, College Park, Maryland 20742, USA*
[3] *Department of Physics, University of Maryland College Park, Maryland 20742, USA*
[4] *Department of Electrical Engineering and Computer Science, Massachusetts Institute of Technology, Cambridge, Massachusetts 02139, USA*
[5] *United States Army Research Laboratory, Adelphi, Maryland 20783, USA*
[6] *Joint Quantum Institute (JQI), University of Maryland, College Park, Maryland 20742, USA*

(Received 29 June 2022; revised 17 December 2022; accepted 7 February 2023; published 1 March 2023)

Trapped ions are promising candidates for nodes of a scalable quantum network due to their long-lived qubit coherence times and high-fidelity single- and two-qubit gates. Future quantum networks based on trapped ions will require a scalable way to route photons between different nodes. Photonic integrated circuits from fabrication foundries provide a compact solution to this problem. However, these circuits typically operate at telecommunication wavelengths that are incompatible with the strong dipole emissions of trapped ions. In this work, we demonstrate the routing of single photons from a trapped ion using a photonic integrated circuit. We employ quantum frequency conversion to match the emission of the ion to the operating wavelength of a foundry-fabricated silicon nitride photonic integrated circuit, achieving a total transmission of $31.0\% \pm 0.9\%$ through the device. Using programmable phase shifters, we switch the single photons between the output channels of the circuit and demonstrate a 50:50 beam splitting condition. These results constitute an important step towards programmable routing and entanglement distribution in large-scale quantum networks and distributed quantum computers.

DOI: 10.1103/PhysRevApplied.19.034001

I. INTRODUCTION

Trapped ions excel as a platform for quantum networking [1–6]. They exhibit long qubit coherence times [7], high-fidelity single- and two-qubit gates [8,9], and the ability to generate single photons entangled with their internal qubit states [3,4,10,11]. Moreover, they can be trapped in compact surface traps [12,13] with integrated waveguides and grating couplers to deliver the light required for cooling and coherent operations [14–16] and close-proximity detectors for state detection [17]. However, integrating these discrete memories into a quantum network requires scalable methods to route single photons between different network nodes [1,18].

Integrated photonic devices offer a compact and scalable solution to realize quantum interconnects that can route photons between nodes of a trapped-ion quantum network [19,20]. These devices can act as reconfigurable optical cross-connect switches that control the path of photonic qubits within the network in a programmable way [1,18]. However, the use of integrated photonics to route photons from trapped ions has remained a challenge because their emission typically lies in the ultraviolet and visible wavelength regimes [3,10,11,21,22]. This emission is incompatible with the majority of active photonic integrated circuit platforms, which are mainly designed to work at telecommunication wavelengths [23,24].

In this work, we demonstrate the routing of single photons from a trapped ion using a photonic integrated circuit designed to operate at the telecom C band. To convert the visible wavelength emission of the ion to the single-mode operating condition of the photonic integrated circuit, we employ a two-stage quantum frequency conversion process [25]. We actively route photons between different output ports of the circuit with a total transmission of $31.0\% \pm 0.9\%$ through the device. We also implement 50:50 beam splitting, an essential operation for entanglement distribution [1,3,18,26]. Our photonic integrated circuit is fabricated using a commercial foundry, which is compatible with large scale-up [27,28]. The primary purpose of our device is to distribute entanglement over

---

[*] uday@terpmail.umd.edu
[†] edowaks@umd.edu

a quantum network, as described by Monroe and Kim [1] via probabilistic photon emission with heralded detection. Our demonstration opens the possibilities for quantum networks where single photons distribute entanglement between trapped-ion nodes in a programmable way over long distances with high-yield routers.

II. EXPERIMENTAL DETAILS AND METHODS

Figure 1(a) shows the schematic of the photonic integrated circuit along with an optical microscope image of the device. The device consists of a Mach-Zehnder interferometer composed of two 50:50 directional couplers with a programmable internal phase shifter between them. The external phase shifter at port 1 can be used to adjust the phase difference between output ports, which is important to control two-photon interference when distributing entanglement [29]. In our experiments, we set this phase shifter current to 0 mA. The device is fabricated using the standardized Si_3N_4 LioniX TriPleX® process with optoelectronic packaging and fiber pigtail. The waveguides in the photonic circuit are double-striped silicon nitride waveguides, which exhibit low loss. A full description of the waveguide geometry and LioniX TriPleX fabrication process can be found in Ref. [24]. We control the thermo-optic phase shifters using current-driven chromium heaters on the top of the cladding layer above the waveguide. The interferometer has a scalable width of approximately 250 μm and length of about 5.5 mm. The device is housed on a chip of 8 mm by 32 mm where it is possible to add around 60 more Mach-Zehnder interferometer units.

A. Characterization of the Mach-Zehnder interferometer

We first characterize the transmission behavior of the Mach-Zehnder interferometer with a continuous-wave laser operating at a wavelength of 1534 nm. We couple light into the input port and measure the transmission at the output ports 1 and 2 as a function of the current applied to the internal phase shifter [Fig. 1(b)]. The current on the internal phase shifter changes the refractive index of the material, creating a phase shift between the top and bottom waveguides. By sweeping the current supplied to the phase shifter, we can continuously shift the output light from port 1 to port 2, achieving a near-maximum transmission out of port 2 at the device's current limit of 16.6 mA, specified by LioniX [Fig. 1(b)]. Under this condition, the device draws approximately 200 mW power with a bias voltage of 12 V. We achieve a 50:50 beam splitting ratio with 11.05 mA applied to the internal phase shifter. We determine this current level by finding the point where the red and blue lines intersect with each other in Fig. 1(b).

At the current limit of 16.6 mA, we attain a phase shift ($\Delta\phi$) of 0.82π by fitting the transmission of port 1 to $\cos^2(\Delta\phi)$. Here, the relationship between phase shift and current is given by the relationship $\Delta\phi = (2\pi L/\lambda)\,(dn/dT)(I^2 R_h \tau/H) + \phi_0$ [30,31]. Here $\Delta\phi$ is the phase shift and I represents the current applied in the internal phase shifter. λ is the operating wavelength and (dn/dT) corresponds to the change of refractive index (n) with temperature (T). L, R_h, τ, and H represent the length, resistance, time constant, and heat capacity of the heater, respectively. We define ϕ_0 as the constant phase shift between top and bottom waveguides. Higher currents could increase this phase shift, but would also exceed the

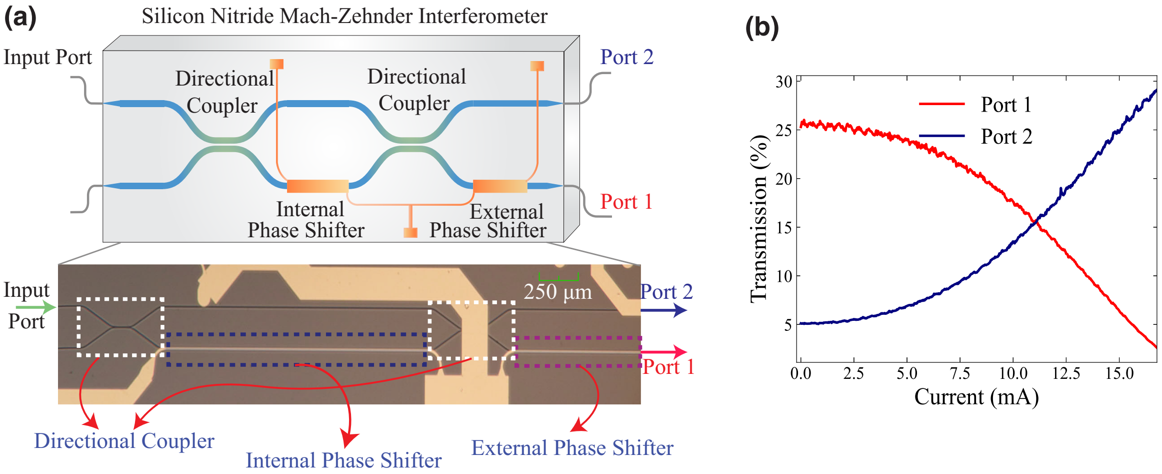

FIG. 1. Schematic and transmission properties of the Mach-Zehnder interferometer. (a) A schematic of the silicon nitride Mach-Zehnder interferometer along with an optical microscope image. Highlighted white, blue, and purple boxes are the two directional couplers and the internal and external phase shifters, respectively. (b) The transmission of the Mach-Zehnder interferometer measured at the two output ports as a function of current applied to the internal phase shifter when laser light is coupled into the input port.

specified damage threshold of the device. This issue can be rectified by increasing the length of the internal phase shifter to achieve a larger phase shift with the same current.

We define the extinction ratio of each output port as the ratio between their maximum and minimum transmission. Using this definition, the extinction ratios are 10.2 dB and 7.6 dB for port 1 and port 2, respectively. These imperfect extinction ratios can be attributed to fabrication imperfections in the directional couplers that alter the process parameters like width, etch depth, gap, thin-film thickness, etc., from their intended design values. These imperfections deviate the directional couplers from their ideal 50:50 ratio, hindering the ability to obtain perfect interference and a high extinction ratio. These imperfections can be mitigated by replacing the directional couplers with active Mach-Zehnder interferometers where the splitting ratio can be actively tuned close to its ideal value [32]. Using this technique, proposed by Miller [32], Wilkes *et al.* demonstrated a 60-dB extinction ratio for an on-chip Mach-Zehnder interferometer [33].

The imbalance in extinction ratios can result from the imbalanced configuration of the Mach-Zehnder interferometer. The heater at the bottom waveguide, which controls the phase shift, creates a loss difference between the top and bottom waveguides in the interferometer, resulting in an imbalance in the extinction ratios. To overcome this imbalance, we could use a balanced configuration of the Mach-Zehnder interferometer by including heaters in both the top and bottom waveguides [34].

The sum of the transmission from the two output ports is 31.0% ± 0.9% for all heater currents. The losses in the device arise from imperfect coupling from the fiber pigtail, waveguide losses, back-reflection, and optical absorption by the metal contact. This transmission is consistent with the expected losses in the device including from the input and output facets (<2 dB/facet), the two heating elements (<0.5 dB each), and the intrinsic material loss (<0.1 dB/cm) specified by LioniX [24].

B. Experimental layout and single photon production

Figure 2(a) shows a block diagram illustration of the experimental setup used to generate single photons from a trapped ion and couple the emission into the photonic integrated circuit. We first generate 493-nm visible single photons from a trapped barium ion (^{138}Ba$^+$). The vacuum chamber housing the ion trap has both a front and back reentrant window, allowing for photon collection in two directions. Photons collected from the back window are sent to a photomultiplier tube to measure the temporal photon shape of 493-nm photons throughout the experiment. Photons collected from the front window are sent through a polarizer and converted to 1534 nm using a two-stage quantum frequency conversion system

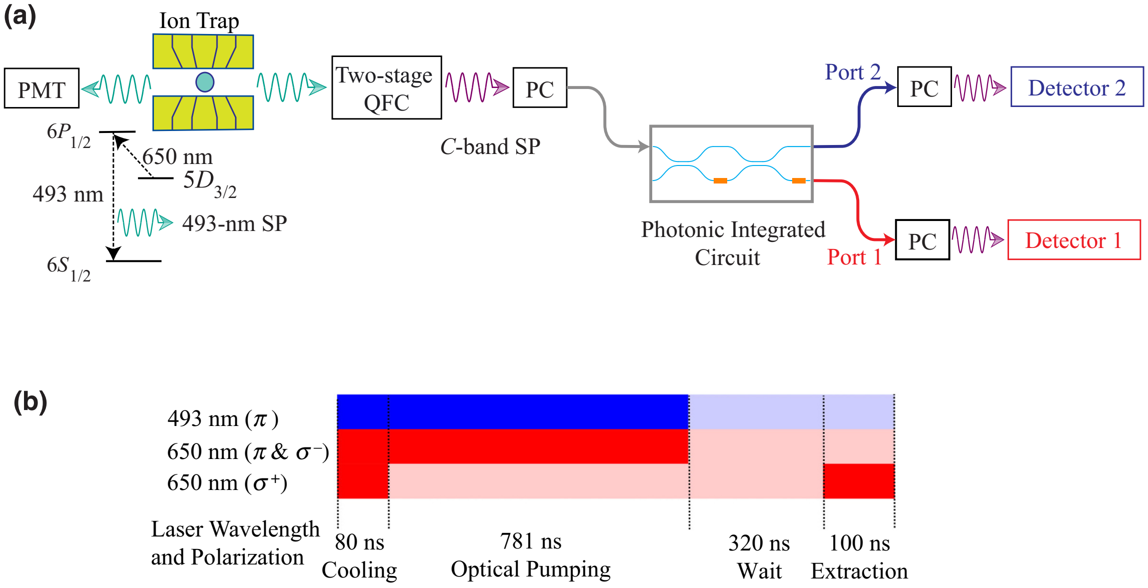

FIG. 2. The experimental layout and timing sequence. (a) Block diagram illustration of the experimental setup used to route single photons from a trapped barium ion using a silicon nitride photonic integrated circuit. Here PMT is photomultiplier tube; QFC is quantum frequency conversion; PC is polarization control; SP is single photon. Also shown is the basic energy level diagram for ^{138}Ba$^+$ depicting the 493-nm and 650-nm transitions and the emission of a single photon with a wavelength of 493 nm. Two-stage QFC includes both the quantum frequency conversion stages and subsequent filtering stage via a 20-GHz-bandwidth tunable filter and 46.1-MHz-bandwidth etalon. (b) The experimental timing sequence showing the wavelength and polarization of the various 493-nm and 650-nm beams that we use to cool, optically pump, and extract single 493-nm photons from the trapped barium ion. In this figure, solid and transparent colors indicate that the lasers are on and off, respectively.

as reported in Ref. [25]. This wavelength is compatible with the single-mode operation of our designed photonic integrated circuit. We then couple converted single photons to the input port of the silicon nitride Mach-Zehnder interferometer. A free-space polarization controller prior to the photonic integrated circuit's input fiber coupler aligns the polarization of the photon to the transverse electric guided mode of the waveguide. We use two superconducting nanowire single-photon detectors to detect photons at the output ports of the Mach-Zehnder interferometer. Because these detectors are polarization sensitive, we use additional polarization control stages after the output ports to maximize photodetection efficiency.

To generate 493-nm single photons from a single barium ion ($^{138}\mathrm{Ba}^+$), we use a scheme as described in prior work [11,22,25]. First, we Doppler cool the barium ion and then optically pump it into the $|5D_{3/2}, m_j = +3/2\rangle$ state using π and $\sigma-$ polarized 650-nm light and π polarized 493-nm light [6,11,22,25]. We then excite the ion using $\sigma+$ polarized 650-nm light to the $|6P_{1/2}, m_j = +1/2\rangle$ state, which can spontaneously decay to the $|6S_{1/2}, m_j = \pm 1/2\rangle$ ground state, emitting a 493-nm single photon. This process is repeated at a rate of 780.64 kHz and the relative timings of this sequence are shown in Fig. 2(b). In this figure, the solid color represents the corresponding laser being on, whereas the transparent color indicates the laser is off. In each cycle of photon production, we wait for 320 ns, directly after optical pumping, with all the lasers being off, to ensure that no stray light is detected during the photon extraction process. The dedicated Doppler-cooling time of 80 ns prioritizes the photon production rate over achieving a low ion temperature. That is, the value chosen is the lowest possible time that does not produce a measurable degradation in the emitted photon's coupling into the single-mode fiber after the collection lens.

C. Quantum frequency conversion

We use a two-stage quantum frequency conversion scheme to generate telecom *C*-band photons from the ion. Quantum frequency conversion is the process where the quantum states of two light beams of different frequencies can be interchanged [35]. In quantum frequency conversion, the noise and other parasitic processes are reduced to an extremely low level such that the frequency conversion process preserves the quantum nature of the light [35]. We reported the details of the quantum frequency conversion system in previous work [25]. In the first stage of quantum frequency conversion, we generate 780-nm single photons from 493-nm single photons utilizing a 1343-nm pump laser with a conversion efficiency of 20% including filtering at around 220-mW pump power [36,37]. Then, in a second stage of conversion, we convert 780-nm single photons to 1534-nm single photons using a 1589-nm pump laser. We achieve 25% conversion efficiency in the second stage of quantum frequency conversion including all filtering at around 250-mW pump power. To filter anti-Stokes noise photons produced by spontaneous Raman scattering from the 1589-nm pump laser, we use a 20-GHz-bandwidth tunable filter with 80% transmission, and a 46.1-MHz-bandwidth etalon with approximately 60% transmission after the second stage. In both frequency conversion processes, we use a difference frequency generation scheme using periodically poled lithium niobate waveguides [25,36]. We attain an overall conversion efficiency of 5% in the two-stage frequency conversion scheme.

To stabilize the frequency of the *C*-band converted photon, we lock the two pump laser frequencies to ensure that the converted photons do not drift outside the bandwidth of the etalon. We first lock a 1762-nm laser to an ultralow expansion cavity via a Pound-Drever-Hall technique. This locked laser is then used as a reference laser with which we lock the conversion pump lasers. We lock the pump lasers relative to the 1762-nm laser using a Fabry-Perot scanning cavity [38] with a scan frequency of 170 Hz resulting in a drift lock of a few megahertz.

III. RESULTS

Figure 3 shows the time-resolved photon counts at the output ports, relative to a trigger pulse synchronized with the extraction laser pulse. All data are background-subtracted to account for detector dark counts and Raman anti-Stokes noise photons created by the pump laser in the conversion process. The dark counts of detectors 1 and 2 are around 110 ± 20 and 150 ± 20 counts/sec, respectively. The pump used in the second stage of quantum frequency conversion produces noise photons due to undesirable processes such as Raman scattering of the pump. As a result, we detect about 2350 ± 50 counts/sec noise photons, measured at the output of the filters to the two-stage conversion and before the photonic integrated circuit using detector 1. This noise is dominated by Raman anti-Stokes noise photons present in the bandwidth of the filtering after two-stage quantum frequency conversion. The proportion of the Raman anti-Stokes noise photons present in each detector channel can be found by considering the respective channel's transmission from the Mach-Zehnder interferometer.

Figure 3(a) shows the time-resolved photon counts measured at port 1 when the current of the internal phase shifter is set to 0 mA (red circles). The two vertical green dashed lines denote the time window used to measure the photon arrival events. We determine this time window from the temporal shape of the 493-nm photons measured using the photomultiplier tube. We set the window width to be 32 ns, which captures 75% of the total 493-nm photon counts. The red data points show the *C*-band converted

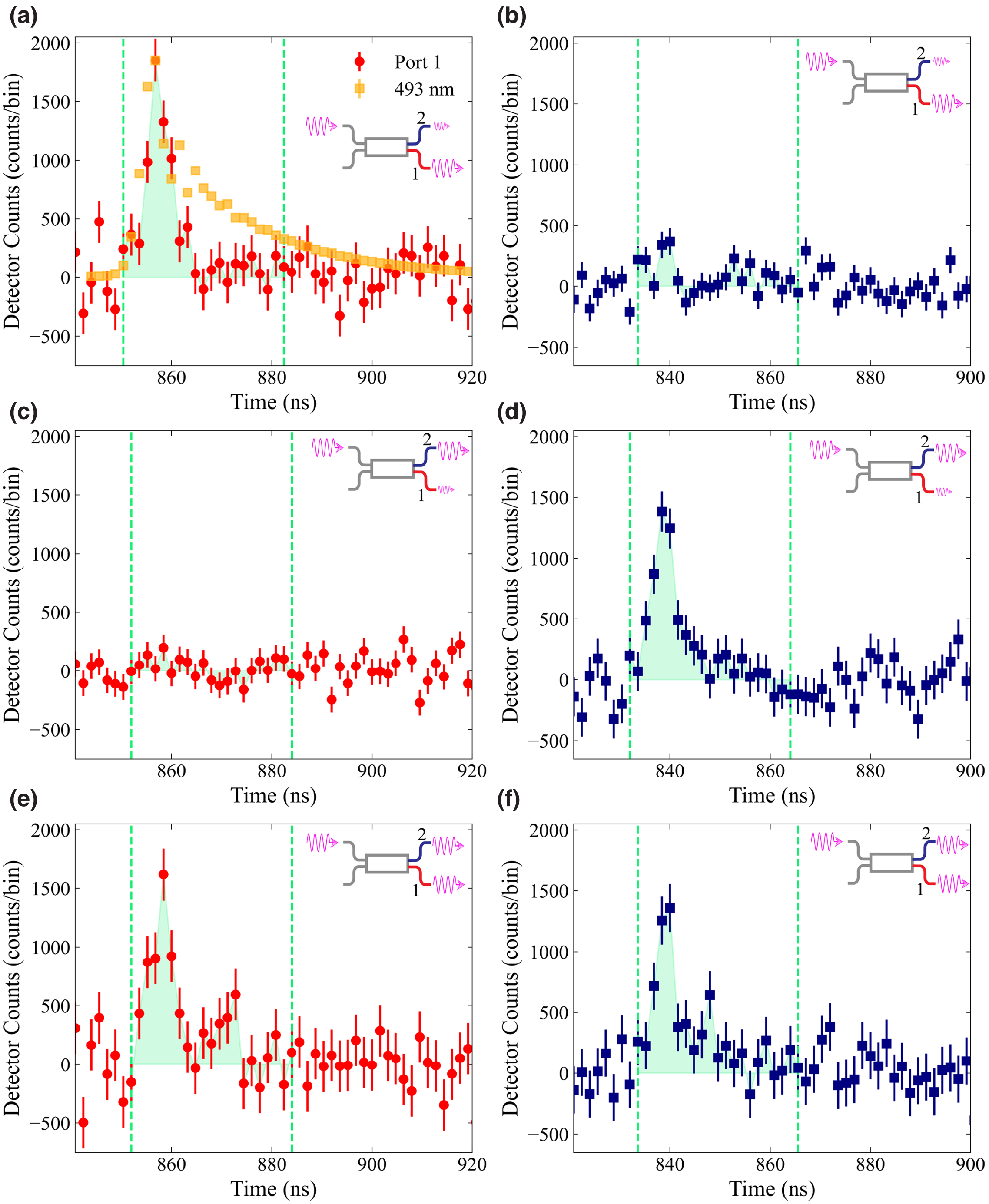

FIG. 3. The temporal photon shapes at the output ports of the Mach-Zehnder interferometer at different current levels of the internal phase shifter. (a),(b) Time-resolved photon counts at port 1 (red circles) and port 2 (blue squares) when the interferometer is set at the maximum transmission of port 1 (0 mA current on the internal phase shifter). In these plots, the horizontal axis shows the time difference between the arrival of the photon and the trigger pulse. We also plot the scaled version of 493-nm time-resolved photon counts (gold squares) as a reference. (c),(d) Time-resolved photon counts measured at port 1 and port 2 when the internal phase shifter current is set to have nearly maximum transmission at port 2 (16.6 mA current on the internal phase shifter). (e),(f) Time-resolved photon counts measured at port 1 and port 2 for a 50:50 beam splitting condition of the Mach-Zehnder interferometer (11.05 mA current on the internal phase shifter). The green vertical lines in all plots indicate the window used to count photon arrival events and correspond to 75% of the total 493-nm time-resolved photon counts. The green shaded area represents the photon area measured at each output port. We use a 1.6-ns bin size and perform background subtraction to plot all the time-resolved photon counts. All errors correspond to shot-noise-limited accuracy. The run times for the current condition of 0 mA [(a),(b)], 16.6 mA [(c),(d)], and 11.05 mA [(e),(f)] are 10.34 h, 9.56 h, and 19.44 h, respectively.

photon signal during the window, consistent with the time-resolved 493-nm photon counts (gold squares). Figure 3(b) shows the same trace for *C*-band converted photons at port 2 (blue squares). In this case, the histogram shows a large reduction in photon probability, indicating that nearly all single photons are routed to port 1. Figures 3(c) and 3(d) show the same measurements at an internal phase shifter current of 16.6 mA, which corresponds to the reverse condition. Here, the majority of photons exit at port 2, and we observe only a weak signal at port 1. These measurements demonstrate the routing of single photons from a trapped ion to different output ports of the photonic integrated circuit. Figures 3(e) and 3(f) show the time-resolved photon counts at output ports 1 and 2, respectively, when we apply a current of 11.05 mA to the internal phase shifter, which corresponds to the 50:50 beam splitting condition. In this case, we measure the time-resolved photon counts at both ports with similar amplitudes. The run time for data taken with the photonic integrated device's internal shifter set to 0 mA [Figs. 3(a) and 3(b)], 16.6 mA [Figs. 3(c) and 3(d)], and 11.05 mA [Figs. 3(e) and 3(f)] are 10.34 h, 9.56 h, and 19.44 h, respectively. Using the peak counts/bin shown in Fig. 3 and the run times, we get a total count rate within the peak bin of 179 counts/h, 145 counts/h, and 153 counts/h for the three current conditions, with variations attributed to different alignment settings between days.

Figure 4 shows the splitting ratios of port 1 and port 2 measured using the photon areas in Fig. 3 (red circles and blue squares, respectively), superimposed over the measured splitting ratio using a continuous wave laser (red and blue dotted lines). We calculate the splitting ratios by dividing the counts at each output port by the sum of the counts at both ports. These values are corrected for mismatch of the photodetection efficiencies between the detectors at port 1 and port 2. The ratio of detection efficiency of the detector at port 1 to that at port 2 is 1.13 ± 0.07, with fiber coupling and polarization control losses taken into account. The error bars correspond to the shot-noise-limited accuracy based on the photon counts in each measurement. The splitting ratios calculated from the photon shapes show good agreement with the transmission ratios measured with classical laser light, within experimental uncertainties. These measurements confirm that we are able to route single photons from the ion using the photonic integrated circuit in a programmable manner.

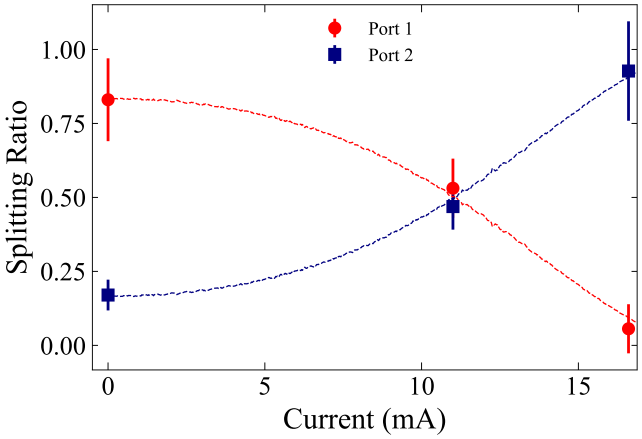

FIG. 4. The splitting ratio of the output ports of the Mach-Zehnder interferometer as a function of current applied to the internal phase shifter. The data points represent the splitting ratio calculated from the background-corrected time-resolved photon counts in Fig. 3. The error bars are calculated from the shot noise of the photon counts. The dotted red and blue lines show the splitting ratio of ports 1 and 2 measured using classical laser light calculated using the data in Fig 1(b).

IV. DISCUSSION

In summary, we demonstrate programmable switching of single photons emitted from a trapped ion between different channels on a photonic integrated chip. Our current proof-of-concept demonstration can be extended in future devices in a straightforward way to include large numbers of Mach-Zehnder interferometers to achieve $N \times N$ cross-connects or other arbitrary unitary matrix transformations [29,39]. In addition to routing, photonic integrated circuits can take on other functionalities such as filtering [40], wavelength division multiplexing [41], and frequency conversion [42]. An ultralow-power high-speed switching of photons could be achieved in devices that use the plasma dispersion effect in silicon modulators [43] at the expense of router transmission efficiency. They can also implement fundamental quantum operations such as photonic Bell-state analysis [1,3,18,26], which is necessary to entangle quantum nodes over long distances. These capabilities could ultimately be used to realize scalable and programmable quantum networks using trapped-ion quantum technology.

All the data and codes that support the finding of this study are available from the corresponding author upon request.

ACKNOWLEDGMENTS

We acknowledge the support from LioniX for fabricating the photonic integrated circuit. We would like to acknowledge the support from the National Science Foundation (Grants No. OIA2134891, No. EFMA1741651, and No. OIA2040695) and the Air Force Office of Scientific Research (Grants No. FA95501610421 and No. FA95501810161).

U.S., E.W., and J.D.S. conceived the idea. U.S., M.P., J.D.S., and D.E. designed the experimental layout and photonic integrated circuits. U.S., J.H., and J.D.S. performed the experiment and analyzed the data. All authors contributed to writing, editing, and reviewing the manuscript.

All authors declare no conflict of financial interest.

[1] C. Monroe and J. Kim, Scaling the ion trap quantum processor, Science **339**, 1164 (2013).

[2] L.-M. Duan and C. Monroe, Colloquium: Quantum networks with trapped ions, Rev. Mod. Phys. **82**, 1209 (2010).

[3] L. J. Stephenson, D. P. Nadlinger, B. C. Nichol, S. An, P. Drmota, T. G. Ballance, K. Thirumalai, J. F. Goodwin, D. M. Lucas, and C. J. Ballance, High-Rate, High-Fidelity Entanglement of Qubits Across an Elementary Quantum Network, Phys. Rev. Lett. **124**, 110501 (2020).

[4] M. Bock, P. Eich, S. Kucera, M. Kreis, A. Lenhard, C. Becher, and J. Eschner, High-fidelity entanglement between a trapped ion and a telecom photon via quantum frequency conversion, Nat. Commun. **9**, 1998 (2018).

[5] V. Krutyanskiy, M. Meraner, J. Schupp, V. Krcmarsky, H. Hainzer, and B. P. Lanyon, Light-matter entanglement over 50 km of optical fibre, npj Quantum Inf. **5**, 1 (2019).

[6] A. N. Craddock, J. Hannegan, D. P. Ornelas-Huerta, J. D. Siverns, A. J. Hachtel, E. A. Goldschmidt, J. V. Porto, Q. Quraishi, and S. L. Rolston, Quantum Interference between Photons from an Atomic Ensemble and a Remote Atomic Ion, Phys. Rev. Lett. **123**, 213601 (2019).

[7] P. Wang, C.-Y. Luan, M. Qiao, M. Um, J. Zhang, Y. Wang, X. Yuan, M. Gu, J. Zhang, and K. Kim, Single ion qubit with estimated coherence time exceeding one hour, Nat. Commun. **12**, 233 (2021).

[8] T. P. Harty, D. T. C. Allcock, C. J. Ballance, L. Guidoni, H. A. Janacek, N. M. Linke, D. N. Stacey, and D. M. Lucas, High-Fidelity Preparation, Gates, Memory, and Readout of a Trapped-Ion Quantum Bit, Phys. Rev. Lett. **113**, 220501 (2014).

[9] C. J. Ballance, T. P. Harty, N. M. Linke, M. A. Sepiol, and D. M. Lucas, High-Fidelity Quantum Logic Gates Using Trapped-Ion Hyperfine Qubits, Phys. Rev. Lett. **117**, 060504 (2016).

[10] B. B. Blinov, D. L. Moehring, L.-M. Duan, and C. Monroe, Observation of entanglement between a single trapped atom and a single photon, Nature **428**, 153 (2004).

[11] J. D. Siverns, X. Li, and Q. Quraishi, Ion–photon entanglement and quantum frequency conversion with trapped Ba^+ ions, Appl. Opt. **56**, B222 (2017).

[12] B. Lekitsch, S. Weidt, A. G. Fowler, K. Mølmer, S. J. Devitt, C. Wunderlich, and W. K. Hensinger, Blueprint for a microwave trapped ion quantum computer, Sci. Adv. **3**, e1601540 (2017).

[13] J. D. Siverns and Q. Quraishi, Ion trap architectures and new directions, Quantum Inf. Process. **16**, 314 (2017).

[14] K. K. Mehta, C. D. Bruzewicz, R. McConnell, R. J. Ram, J. M. Sage, and J. Chiaverini, Integrated optical addressing of an ion qubit, Nat. Nanotechnol. **11**, 1066 (2016).

[15] R. J. Niffenegger, J. Stuart, C. Sorace-Agaskar, D. Kharas, S. Bramhavar, C. D. Bruzewicz, W. Loh, R. T. Maxson, R. McConnell, D. Reens, *et al.*, Integrated multi-wavelength control of an ion qubit, Nature **586**, 538 (2020).

[16] K. K. Mehta, C. Zhang, M. Malinowski, T.-L. Nguyen, M. Stadler, and J. P. Home, Integrated optical multi-ion quantum logic, Nature **586**, 533 (2020).

[17] S. L. Todaro, V. B. Verma, K. C. McCormick, D. T. C. Allcock, R. P. Mirin, D. J. Wineland, S. W. Nam, A. C. Wilson, D. Leibfried, and D. H. Slichter, State Readout of a Trapped Ion Qubit Using a Trap-Integrated Superconducting Photon Detector, Phys. Rev. Lett. **126**, 010501 (2021).

[18] C. Monroe, R. Raussendorf, A. Ruthven, K. R. Brown, P. Maunz, L.-M. Duan, and J. Kim, Large-scale modular quantum-computer architecture with atomic memory and photonic interconnects, Phys. Rev. A **89**, 022317 (2014).

[19] J. Wang, F. Sciarrino, A. Laing, and M. G. Thompson, Integrated photonic quantum technologies, Nat. Photonics **14**, 273 (2019).

[20] U. Saha and E. Waks, Design of an integrated Bell-state analyzer on a thin-film lithium niobate platform, IEEE Photonics J. **14**, 1 (2022).

[21] P. Kobel, M. Breyer, and M. Köhl, Deterministic spin-photon entanglement from a trapped ion in a fiber Fabry–Perot cavity, npj Quantum Inf. **7**, 1 (2021).

[22] C. Crocker, M. Lichtman, K. Sosnova, A. Carter, S. Scarano, and C. Monroe, High purity single photons entangled with an atomic qubit, Opt. Express **27**, 28143 (2019).

[23] A. E.-J. Lim, J. Song, Q. Fang, C. Li, X. Tu, N. Duan, K. K. Chen, R. P.-C. Tern, and T.-Y. Liow, Review of silicon photonics foundry efforts, IEEE J. Sel. Top. Quantum Electron. **20**, 405 (2014).

[24] C. G. H. Roeloffzen, M. Hoekman, E. J. Klein, L. S. Wevers, R. B. Timens, D. Marchenko, D. Geskus, R. Dekker, A. Alippi, R. Grootjans, *et al.*, Low-loss $\mathrm{Si_3N_4}$ TriPleX optical waveguides: Technology and applications overview, IEEE J. Sel. Top. Quantum Electron. **24**, 1 (2018).

[25] J. Hannegan, U. Saha, J. D. Siverns, J. Cassell, E. Waks, and Q. Quraishi, C-band single photons from a trapped ion via two-stage frequency conversion, Appl. Phys. Lett. **119**, 084001 (2021).

[26] D. L. Moehring, P. Maunz, S. Olmschenk, K. C. Younge, D. N. Matsukevich, L.-M. Duan, and C. Monroe, Entanglement of single-atom quantum bits at a distance, Nature **449**, 68 (2007).

[27] W. Bogaerts, Y. Xing, and U. Khan, Layout-aware variability analysis, yield prediction, and optimization in photonic integrated circuits, IEEE J. Sel. Top. Quantum Electron. **25**, 1 (2019).

[28] P. Muñoz, P. W. L. van Dijk, D. Geuzebroek, M. Geiselmann, C. Domínguez, A. Stassen, J. D. Doménech, M. Zervas, A. Leinse, C. G. H. Roeloffzen, *et al.*, Foundry developments toward silicon nitride photonics from visible to the mid-infrared, IEEE J. Sel. Top. Quantum Electron. **25**, 1 (2019).

[29] N. C. Harris, G. R. Steinbrecher, M. Prabhu, Y. Lahini, J. Mower, D. Bunandar, C. Chen, F. N. C. Wong, T. Baehr-Jones, M. Hochberg, *et al.*, Quantum transport simulations in a programmable nanophotonic processor, Nat. Photonics **11**, 447 (2017).

[30] M. Prabhu, *Towards Optimal Capacity-Achieving Transceivers with Photonic Integrated Circuits* (Massachusetts Institute of Technology, Cambridge, 2018).

[31] N. C. Harris, Y. Ma, J. Mower, T. Baehr-Jones, D. Englund, M. Hochberg, and C. Galland, Efficient, compact and low loss thermo-optic phase shifter in silicon, Opt. Express **22**, 10487 (2014).

[32] D. A. B. Miller, Perfect Optics with Imperfect Components, Optica **2**, 747 (2015).

[33] Wilkes, Qiang, Wang, Santagati, and Paesani, 60 dB high-extinction auto-configured Mach–Zehnder interferometer, Opt. Lett. **41**, 5318 (2016).

[34] Y. Shen, N. C. Harris, S. Skirlo, M. Prabhu, T. Baehr-Jones, M. Hochberg, X. Sun, S. Zhao, H. Larochelle, D. Englund, and M. Soljačić, Deep learning with coherent nanophotonic circuits, Nat. Photonics **11**, 441 (2017).

[35] P. Kumar, Quantum frequency conversion, Opt. Lett. **15**, 1476 (1990).

[36] J. D. Siverns, J. Hannegan, and Q. Quraishi, Neutral-Atom Wavelength-Compatible 780 Nm Single Photons from a Trapped Ion via Quantum Frequency Conversion, Phys. Rev. Appl. **11**, 014044 (2019).

[37] J. D. Siverns, J. Hannegan, and Q. Quraishi, Demonstration of slow light in rubidium vapor using single photons from a trapped ion, Sci Adv **5**, eaav4651 (2019).

[38] J. J. McLoughlin, A. H. Nizamani, J. D. Siverns, R. C. Sterling, M. D. Hughes, B. Lekitsch, B. Stein, S. Weidt, and W. K. Hensinger, Versatile ytterbium ion trap experiment for operation of scalable ion-trap chips with motional heating and transition-frequency measurements, Phys. Rev. A **83**, 013406 (2011).

[39] W. R. Clements, P. C. Humphreys, B. J. Metcalf, W. Steven Kolthammer, and I. A. Walmsley, Optimal design for universal multiport interferometers, Optica **3**, 1460 (2016).

[40] W. Bogaerts, P. De Heyn, T. Van Vaerenbergh, K. De Vos, S. Kumar Selvaraja, T. Claes, P. Dumon, P. Bienstman, D. Van Thourhout, and R. Baets, Silicon microring resonators, Laser Photonics Rev. **6**, 47 (2012).

[41] C. A. Brackett, Dense wavelength division multiplexing networks: Principles and applications, IEEE J. Sel. Areas Commun. **8**, 948 (1990).

[42] Y. Hu, M. Yu, D. Zhu, N. Sinclair, A. Shams-Ansari, L. Shao, J. Holzgrafe, E. Puma, M. Zhang, and M. Lončar, On-chip electro-optic frequency shifters and beam splitters, Nature **599**, 587 (2021).

[43] W. M. Green, M. J. Rooks, L. Sekaric, and Y. A. Vlasov, Ultra-Compact, Low RF Power, 10 Gb/s Silicon Mach-Zehnder Modulator, Opt. Express **15**, 17106 (2007).